10924 *Ind. Eng. Chem. Res.* **2010,** *49,* 10924–10933

Micro-Scale Catalytic Reactor for Syngas Production

S. Vaccaro,* L. Malangone, and P. Ciambelli

Department of Chemical and Food Engineering, University of Salerno,
Via ponte don Melillo 84084 - Fisciano (SA) Italy

This paper presents both experimental and modeling investigations of a catalytic wall fuel processor consisting of coupled methane reforming and methane combustion sections. The reacting systems are both catalytic and the latter generates the heat required for the occurrence of the former. The catalytic wall reactor was examined for light-off behavior and for steady-state product distribution. On one hand, the analysis of the reaction products distribution after catalyst ignition indicated that in both combustion and reforming sections catalysts undergo to a relatively long transient (about 40 min) before reaching steady state conditions. On the other hand, a much longer reactor thermal transient was observed and the two transient behaviors appear independent of each other. Analysis of the reactor operating under real conditions (nonadiabatic) showed that a 3D model is needed to accurately predict the reactor performance because a 2D model, although much more convenient, cannot allow for the whole heat loss thereby yielding unreliable results.

1. Introduction

The trigger for the marked diffusion of research activities in the field of microscale systems for hydrogen production derived from their potential to yield ideal performance for on-board fuel processors. In fact, reforming in microscale reactors may enable extremely high mass and heat transport rates and, therefore, the use of small and compact devices with good dynamic behavior, high conversion efficiency, and relatively small energy losses.[1]

In the effectiveness of microscale systems for hydrogen production several variables can play a role. The first is the process type. Indeed, although the fuel reforming reactions make up the basic processing step, this can be accomplished in several ways and, consequently, the fuel processor can be built in a variety of configurations: (i) as partial oxidation reactor, which operates exothermically; (ii) as steam reforming reactor, which operates endothermically; (iii) as autothermal reformer (ATR), which ideally combines partial oxidation and steam reforming within the same catalyst bed to ensure thermally neutral operation.[2,3] In many respects a catalytic wall fuel processor consisting of coupled but separated methane reforming and methane combustion sections could be considered as a variant of an ATR. In any event, each of the three reforming routes presents advantages and disadvantages related to various aspects such as startup time, product purity, and complexity of the reactor.

Another relevant variable for hydrogen production in microscale systems is the type of employed fuel. Much of the recent work on fuel processors is focused on the employment of surrogate fuels, biofuels, gasoline, and diesel,[4−8] and on JP8 fuel.[9−12] All of these have a high energy density and, in addition, gasoline and diesel may draw benefit from a developed delivery infrastructure. Nevertheless, the risk of residues and soot formation, with the consequent decline of the catalyst performance, increases with the complexity of the fuel and is, then, a challenge for gasoline and diesel fuel reforming. In this respect the use of simpler fuels such as methane and/or LPG appears much more convenient. In fact, with the use of higher fuel components coking and aging of the catalyst as well as coke formation downstream the reformer from precursors formed in the reformer are major challenges in practical realizations of on-board reformers. The formation of coke precursors is contributed to homogeneous gas-phase reactions, in particular at fuel-rich operating conditions, i.e., molar C/O ratios above unity.[13] The use of higher hydrocarbons poses additional challenges because of their sulfur content, which requires tolerant catalysts and carriers.[14,15]

A further relevant aspect of microscale systems for hydrogen production is the effective thermal efficiency obtainable in a real application. Microreactors convert fuel into a synthesis gas mixture rich in H_2 by utilizing the reaction enthalpy provided by exothermic oxidation reactions to run endothermic ones. Although a standard operation is ideally achieved by adjusting the ratio between combusted and reformed fuel, this is never attained in practice. The enthalpy provided by the combustion reaction of the fuel must allow for unavoidable heat-losses, which are typical for high temperature units, as well as in the case of ATR a selectivity penalty due to competing reactions. Hence, the reactor is required to operate with an excess fuel input compared to the thermally neutral case.[16] The thermal imbalance between exothermic and endothermic reactions generates axial temperature profiles.[17,18] In fact, since the exothermic reactions are much faster than the endothermic ones and take place in the upstream portion of the reactor, the endothermic reactions are unable to locally utilize all of the energy released to ensure thermal neutrality. This results in a high reactor temperature upstream and a temperature decrease in the downstream portion of the reactor. The endothermic reactions rely on heat transported downstream by convection and conduction, as well as radiation from the reactor walls.[2] Similar considerations may be drawn for the variant ATR process, cited above, although the coupling through the catalytic wall of the exothermic and endothermic reactions may attenuate such problems.

Plate-type reactors and microchannel reactors with microstructured catalysts have been proposed for the steam reforming of hydrocarbons.[19−22] In such reactors the knowledge of the temperature profiles is fundamental for designing the catalysts and the reactor geometry. However, given the difficulty of measuring the temperature inside the catalyst structures and evaluating not only the temperature profiles but the whole reactor performance, accurate descriptive or predictive models are

---

* To whom correspondence should be addressed. E-mail: svaccaro@unisa.it.

10.1021/ie100464b

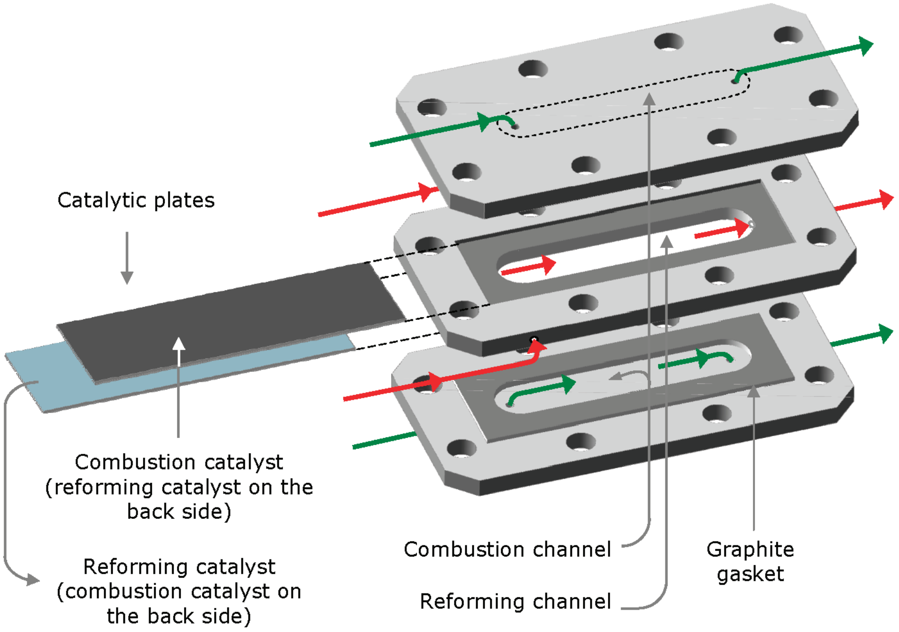

Figure 1. Exploded reactor CAD-view. Green arrows: combustion stream; red arrows: reforming stream.

necessary.[22] In fact, several modeling studies of methane steam reforming in plate-type reactors are reported in the literature[19,21−26] while a comprehensive survey of experimental and modeling works on catalytic plate reactors for combined exothermic and endothermic reactions has been made by Zanfir and Gavriidilis.[19] Some of them[22−24,26] are based on a simplified one-dimensional approach and are used to study mainly axial temperature profiles. Two-dimensional models,[19,21,25] instead, are more realistic and increased the capability to evaluate the effect of wall thickness and channel width, and eliminate the uncertainties introduced by heat and mass transfer coefficients used in one-dimensional models. However, even two-dimensional models included marked simplifying assumptions. For instance, Zanfir and Gavriilidis[19] adopted a two-dimensional geometry for the gas phase and the solid wall, while the catalyst layers were modeled by one-dimensional approach. Fully developed laminar flow was assumed in both endothermic and exothermic channels. In addition, due to its small thickness, the catalyst layer was considered isothermal in the transverse direction and the pressure drop along the channels was neglected.

We recently proposed for the system in the object both 2D and 3D models,[27,28] which eliminate the simplifications reported above and also avoid the use of heat and mass transfer coefficients since the transport phenomena were taken into account by the fundamental transport equations. We found, however, that under the hypothesis of adiabatic operation of the reactor, 2D and 3D models yield practically the same results.[28]

In the context above the present work reports the results of experimental and modeling investigations of a catalytic wall microscale reactor consisting of coupled methane reforming and combustion sections. With respect to previous literature studies on the same topic the intent of this paper was not to present a new reactor configuration but to highlight the relevance of the transient behavior of the reactor and the necessity of a 3D modeling approach when the predictions of the performance of a nonadiabatic device (real operation) are required. To this end, the transient behavior of the reacting system has been studied through the analysis of the temperature and product distribution during the reactor startup. This represents a relevant aspect in the view of the practical application of the fuel processor. Then, the performance of the reactor at steady state has been tested. Furthermore, the study has been focused on the ability of the model to simulate experimental results of catalytic-phase reactions both in the combustion and reforming sections of the reactor. In particular, numerical simulations using 2D and 3D models have been performed to compare their capability to predict the performance of the real reactor where heat losses through the walls are unavoidable. To this end, the longitudinal and transverse temperature profiles in the reactor and the product compositions at the reactor outlet have been compared with the measured ones.

2. Experimental Setup

The experimental setup includes the system for the reactants feed, the reactor, and the devices for product analysis. The reactants for the exothermic and the endothermic reactions can be fed in concurrent (CNC) or counter current (CTC) mode. However, in this paper only results obtained under CNC operating mode are reported. Cylinder air and methane were delivered and metered by mass-flow controllers (Brooks SL5800) while the feedwater flow was regulated by a peristaltic pump (Gilson). The entering reactants streams and the reactor itself were preheated at about 600 °C by electrical heaters and related temperature controllers. The whole reactor and the related tubing were enveloped in a rock wool blanket to provide thermal insulation. The reactor exhaust products concentrations were monitored by ADVANCE OPTIMA, ABB analyzers: specifically, CH_4, CO, and CO_2 by a NDIR analyzer (Uras 14), O_2 by a paramagnetic analyzer (Magnos 106), and H_2 by a thermo-conductivity analyzer (Caldos 17). Gas streams exiting from the reactor were cooled below 0 °C to eliminate the water before being analyzed for species concentration.

In Figure 1 a CAD-view of the catalytic plate reactor is depicted. The reactor, designed to be modular, is made of three stainless steel plates assembled together.

The reforming channel (50 mm long, 10 mm wide, 3.0 mm thick) is shaped inside the inner plate while the combustion channels (50 mm long, 10 mm wide, 1.5 mm thick each) are

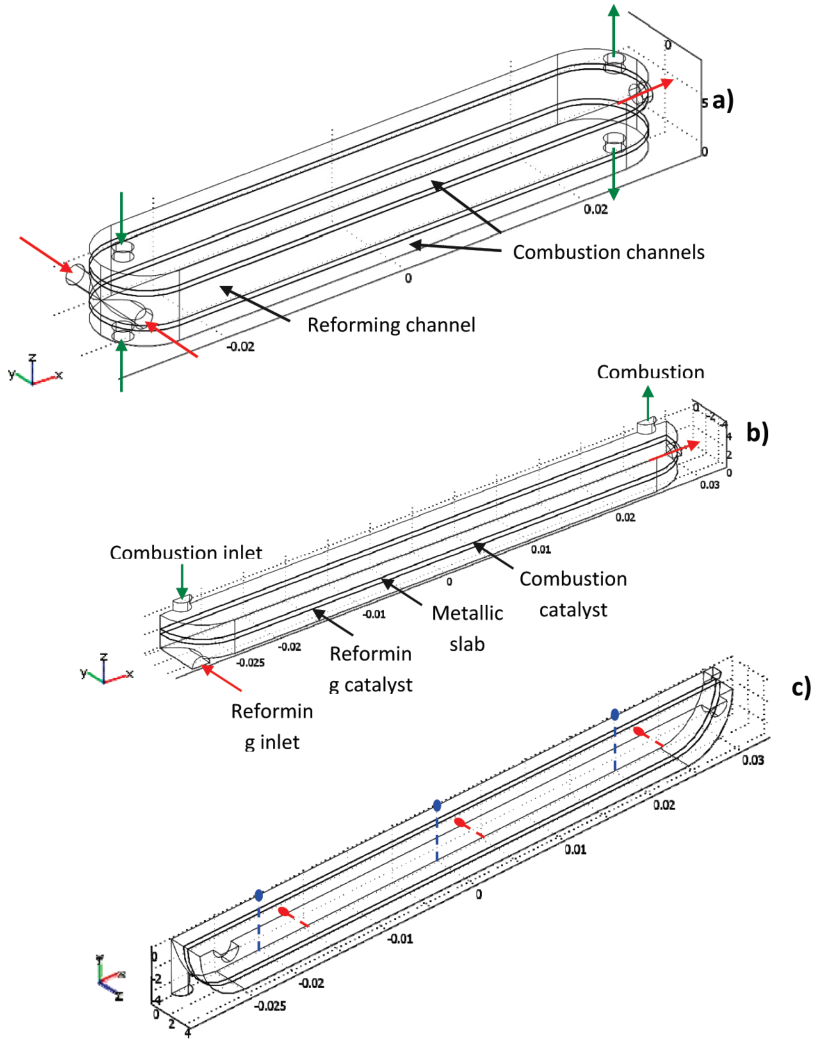

Figure 2. 3D scheme of the reactor. (a) Whole assembly of the modeled reactor including channels, catalyst layers, and inlet and outlet openings; (b) actually modeled portion of the reactor (one-fourth of the complete reactor, i.e, (a)); and (c) positions of the thermocouples inside the reactor: red line, combustion thermocouples; blue lines, reforming thermocouples.

located inside the outer plates. The channels have a parallelepiped shape with two protruding rounded edges (which makes the total channel length 60 mm) and are separated by foils (0.5 mm thick) onto which different catalysts were deposited on the opposite faces (Figure 1). The reactants flow pattern is shown in Figure 1 by arrows: red and green lines represent combustion and reforming streams, respectively. Graphite foils were used as gaskets between the catalytic foils and the stainless steel plates.

Aluchrom slabs (0.5 mm thick; 70% Fe, 25% Cr, 5% Al), supplied by ECOCAT, were used as structured metallic supports. They were formed into rectangular shape (70 × 20 mm^2) to be lodged in the reactor slots and thermally pretreated before washcoating procedure. After cleaning with acetone to remove the superficial impurities, an oxidative pretreatment for the segregation of an Al_2O_3 layer on the metallic surface was carried out at 1200 °C for 10 min in 0.5 vol % O_2 in N_2 stream.[29]

The structured catalysts were prepared using the following: commercial catalytic washcoat (aqueous suspension of 38.5 wt % γ-alumina powder) supplied by ECOCAT, $Ni(NO_3)2\cdot 6H_2O$, as active specie precursor promoting the steam reforming reaction, and $PtCl_4$, as active specie precursor promoting the catalytic combustion reaction both supplied by Carlo Erba Reagenti. The right amount of salt containing the noble metal species was carefully dissolved in the washcoat suspension and then deposited on the pretreated aluchrom foils by brushing. Drying at 60 °C for 4 h and calcination at 950 °C for 2.5 h were then performed. The procedure was repeated for the deposition of a second catalyst layer giving a final coating about 80 μm thick. The complete procedure was also repeated for the deposition of the reforming catalyst on the other side of the slab. A catalytic washcoat containing 5 wt % Ni for the steam reforming reaction and a catalytic washcoat containing 3 wt % Pt for the catalytic combustion reaction were obtained.

Reforming catalyst reduction was accomplished by treatment with 20 L/h at STP of a 5% H_2 in N_2 stream.

The gas temperatures were measured in each channel by three 1.0-mm diameter thermocouples located at distances from one channel edge of 10, 30, and 50 mm, respectively. In addition, each group of the three thermocouples was positioned on the correspondent channel longitudinal axis. Specifically, the thermocouples for the combustion channels were inserted parallel to the z axis (see Figure 2) and those for the reforming channel were inserted parallel to the y axis (see Figure 2).

3. Modeling

3.1. Model. We have developed a 3-D heterogeneous steady-state model[27,28] to describe velocity, concentration, and temperature distributions inside the catalytic slabs reactor. The model consists of the material, energy, and momentum balances equations for the system in the object and contains the constitutive equations for physical chemistry properties of the reactants species and the kinetic expressions for the reactions as found from the literature.[30]

In the present work we used the same model, with minor changes reported below. In addition, the rate equations for the methane steam reforming reactions (eqs 1 and 3) and the water gas shift reaction (eq 2) are those derived by Hou and Hughes[31] on the basis of experiments carried out at 120 kPa for a catalyst containing 15−17% NiO supported on α-Al_2O_3. This model was preferred to the kinetics proposed by Xu and Froment[30] who operated the experiments at a total pressure of 29 bar: this value is characteristic of an industrial process, but is much higher than the operating condition at which our system worked.

$$\mathrm{CH_4 + H_2O{=}CO + 3H_2} \Rightarrow \mathrm{r_1} = \frac{k_1\left(P_{\mathrm{CH_4}}P_{\mathrm{H_2O}}^{0.5}P_{\mathrm{H_2}}^{-1.25}\right)\left(1 - \left(P_{\mathrm{CO}}P_{\mathrm{H_2}}^{3}K_{\mathrm{p1}}^{-1}P_{\mathrm{CH_4}}^{-1}P_{\mathrm{H_2O}}^{-1}\right)\right)}{(\mathrm{den})^2} \quad (1)$$

$$\mathrm{CO + H_2O{=}CO_2 + H_2} \Rightarrow \mathrm{r_2} = \frac{k_2\left(P_{\mathrm{CO}}P_{\mathrm{H_2O}}^{0.5}P_{\mathrm{H_2}}^{-0.5}\right)\left(1 - \left(P_{\mathrm{CO_2}}P_{\mathrm{H_2}}K_{\mathrm{p2}}^{-1}P_{\mathrm{CO}}^{-1}P_{\mathrm{H_2O}}^{-1}\right)\right)}{(\mathrm{den})^2} \quad (2)$$

$$\mathrm{CH_4 + 2H_2O{=}CO_2 + 4H_2} \Rightarrow \mathrm{r_3} = \frac{k_3\left(P_{\mathrm{CH_4}}P_{\mathrm{H_2O}}P_{\mathrm{H_2}}^{-1.75}\right)\left(1 - \left(P_{\mathrm{CO_2}}P_{\mathrm{H_2}}^{4}K_{\mathrm{p3}}^{-1}P_{\mathrm{CH_4}}^{-1}P_{\mathrm{H_2O}}^{-2}\right)\right)}{(\mathrm{den})^2} \quad (3)$$

Where $\mathrm{den} = 1 + K_{\mathrm{CO}}P_{\mathrm{CO}} + K_{\mathrm{H_2}}P_{\mathrm{H_2}}^{0.5} + K_{\mathrm{H_2O}}P_{\mathrm{H_2O}}P_{\mathrm{H_2}}^{-1}$ and k_{i}, K_{pi}, and K_{i} refer to reaction rate constant, equilibrium constant, and adsorption coefficient, respectively.[31] Partial pressures of gases P_i in eqs 1, 2, and 3 were correlated to their own concentrations by the ideal gas law.

For the methane combustion, only the total fuel oxidation to CO_2 was considered: a rate equation depending linearly on the methane concentration only, suggested in the literature[19] for a Pt catalyst, was used. The model, of which a detailed description can be found elsewhere,[28] assumes that: (a) density variations due to change of gas composition and temperature are taken into account by using the weak compressible Navier−Stokes version of the motion equation; (b) on the combustion side only the methane total oxidation reaction to H_2O and CO_2 occurs; (c) on the reforming side only the methane steam reforming and the water gas shift reactions, as schematized by eqs 1, 2, and 3 occur; (d) reactions occur only inside the catalyst layers where, instead, convective momentum is not present; (e) conductive heat transfer is the only transport phenomenon occurring inside the metallic plates; (f) as suggested in the literature,[31] carbon formation and deposition due to side reactions can be neglected by using an excess of steam, that is a steam/methane molar ratio above 1.7; and (g) body forces are neglected.

With respect to the cited model[28] in this work the energy balance and the mass balances for the species involved take into account also the thermal diffusion and the diffusive heat transport which in multicomponent mixtures may be significant.[32] Multicomponent mass transport was modeled using a Fick-like law instead of more complex approaches such as Maxwell Stefan equation or Dusty Gas model to limit computational costs.

A drawing of the modeled portion of the reactor, with the legend of the main component parts, is shown in Figure 2a, b, and c. Figure 2a shows the channels, the inlets and outlets, and the catalytic slabs of the whole device sketched in Figure 1. Figure 2b displays only the actual modeled portion of the reactor, which is one-fourth of the complete reactor (in Figure 2a) because of the symmetries with respect to the $x-y$ and the $x-z$ planes. Finally, Figure 2c, showing a different view of the modeled portion of the reactor, highlights the positions of the thermocouples in the reactor. The reactants flow patterns are also indicated in Figure 2. Both the reforming and the combustion streams enter the reactor along a direction perpendicular to the channel axis (x direction) although the reforming one moves along y and that of combustion moves along z.

According to Figure 2, for each catalyst layer and channel and for the metal foils, the due momentum, energy, and mass balances were set together with the proper boundary conditions in Cartesian coordinates ($x-y-z$) (indicated in Figure 2) with the following dependent variables: velocity components, pressure, temperature (T), and species concentrations (c_i).

3.2. Numerical Parameters and Simulation Conditions. The finite element solution algorithm was completed using COMSOL Multiphysics software (Comsol, Inc., version 3.5). Multiphysics modules of weakly compressible Navier−Stokes, convection−diffusion, and conduction−convection were applied, when appropriate, to the three-phase domains. Due to complexity of the geometry and to improve the resolution of the computed variables, the mesh was properly refined imposing a maximum element size of 0.5×10^{-4} m at the inlet and outlet of both channels and choosing mesh curvature factors accurately; the final mesh consisted of 54004 elements and 689 960 degrees of freedom were solved for. To model the diffusive mass transport inside the catalytic layers, assumed to be 50 μm thick, both molecular and Knudsen diffusion were considered to estimate the effective diffusion constants:[33] the mean pore radius was set equal to 15 nm, while the porosity and tortuosity were 0.5 and 4, respectively.

The methane/oxygen feed ratio employed in the present work was 1/1.68, i.e., above the stoichiometric value (1/2). This because in a previous work the authors found that methane combustion on a Pt based catalyst was inhibited when operating under stoichiometric or excess air condition.[34] This result is also in agreement with literature findings, i.e., when operating with excess air or even under fuel-rich condition but at low temperature, the oxygen adsorption is much faster than methane adsorption. Therefore, in such conditions noble metal surface results mostly covered with O_2 leaving negligible room for CH_4 adsorption.[35−37] A further evidence of such a behavior is that the influence of the oxygen concentration on the kinetics, when using a power-law rate expression, may be neglected according to the literature.[38−41] All this makes clear that to increase the rate of the combustion reaction, it is necessary to increase the methane/oxygen feed ratio well above the stoichiometric ratio.

Methane conversions in the reforming and combustion side ($X_{\mathrm{CH4\text{-}sr}}$ and $X_{\mathrm{CH4\text{-}co}}$, respectively) were calculated on the basis of the measured CH_4 inlet and outlet concentrations. The H_2 yield (φ_{H2}) was evaluated as moles of H_2 produced per mole of CH_4 converted in the reforming channel.

The experimental molar flow rate employed in the experiments, for which results are compared with model predictions, are reported in Table 1.

4. Results and Discussion

4.1. Ignition and Transient. A typical example of the transient behavior of the reactor for what concerns the reaction product distribution is shown in Figure 3 where the species molar fraction on dry basis at the reforming channel outlet is

Table 1. Molar Flow Rates Fed to the Reactor in the Experiments for Which Results Are Compared with Model Predictions

reactant	molar flow rate, mol/min (STP)
$M_{CH4\text{-}co}$	0.0045
$M_{CH4\text{-}sr}$	0.0089
M_{AIR}	0.0357
M_{STEAM}	0.0271

reported as a function of time. Data in Figure 3 show that, upon reactants introduction, the transient to steady state behavior includes two steps: (i) a short delay from reactants introduction in the channels to the reforming and combustion catalyst light-off, and (ii) a quite long transient to reach the steady state products distribution. Specifically, the system takes about 40 min to reach steady state products concentration at the reforming channel outlet.

Typical temperatures time profiles at various locations inside the channels of the reactor are plotted in Figure 4. These values refer to the same test in which the measured products distribution in time are reported in Figure 3. Although there are three thermocouples in each combustion channel, for the sake of clarity in Figure 4 only three values pertaining to the combustion channel are shown. This is also because the temperatures measured in the two combustion channels at corresponding distances from the reactants inlets are practically coincident. Figure 4 shows that, apart from the absolute values, all the temperatures follow the same trend in the time. It is also evident that the reactor reaches steady state temperature only after 110 min after the reactants introduction.

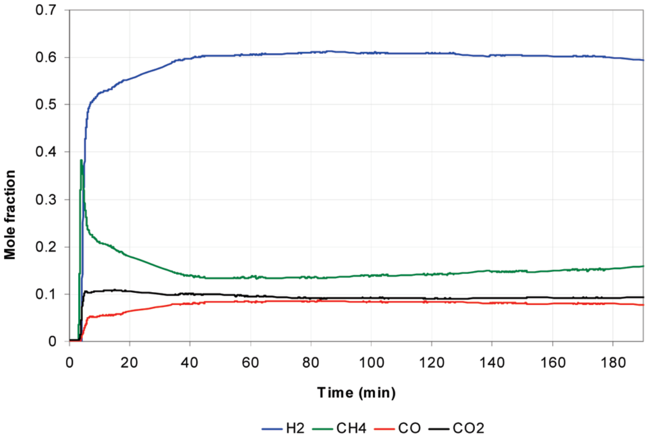

Figure 3. Species concentration on dry basis in the stream at the reforming channel outlet as a function of time from the reactor start up.

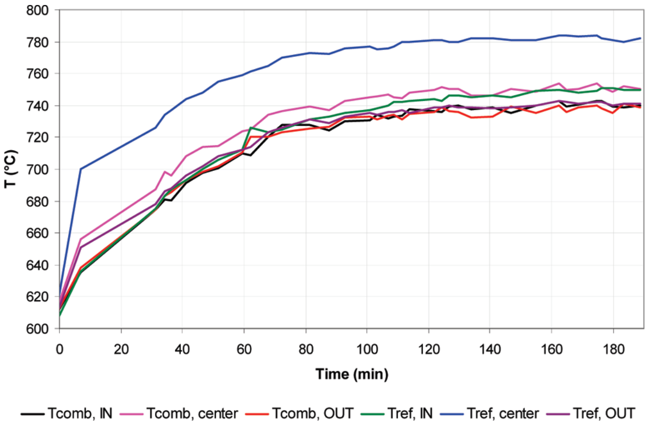

Figure 4. Gas temperature on the reforming and combustion channel axes as a function of time. Distances from the reactants inlet: Ti,in = 1 cm; Ti,center = 3 cm and Ti,out = 5 cm. comb: combustion channel; ref: reforming channel.

The comparison of Figures 3 and 4 suggests that the two transient behaviors should be certainly coupled until there is concentration transient but after they would become uncoupled or at least the second would not depend on the first. At first sight it would seem that the product distribution is insensitive to temperature. However, assuming there is no doubt that the reactants conversion and the extent of the reaction are strongly dependent on the temperature of the reaction zone, we must infer that the reaction zone reaches the steady temperature when the concentration of the reaction products reaches steady state. The confirmation of this interpretation comes from the consideration that, actually, the reactions in the object are catalytic and, then, they do not occur in the whole reactor but only over and inside the catalytic layers and the channels act essentially as gas ducts zone. Therefore, the difference between Figures 3 and 4 in the time necessary to reach steady state may be justified considering that the transient of the species concentration depends mainly on the thermal coupling of the endothermic and exothermic reactions over the catalytic slabs, while the thermal transient depends on the heating of the whole system which, given the considerable mass, needs a longer time to reach steady state condition. In fact, the thermal capacity of the reactor and annex tubing is about 640 J/k. Under steady state condition it is possible to evaluate the rate of heat lost in the environment as the difference between the thermal power produced by the combustion, that consumed by the reforming, and the sensible heat required to heat the entering gas mixture up to the outlet temperature. Assuming as a first approximation that this quantity is lost also during the transient (this assumption is quite correct because the reactor temperature in any case is very high with respect to the room temperature), it is possible to estimate the thermal power remaining to heat the reactor and annex tubing. Dividing the thermal capacity of the reactor for such a quantity we obtain that during the tests more than about 70 s was needed to increase of 1 °C the temperature on the system. This justifies why, after reaching the steady state condition in the composition profiles, the system employs about one more hour to reach the thermal steady state.

To better analyze the temperature distribution in the reactor, results of Figure 4 are reported in a different way in Figure 5. Here, the temperature longitudinal profiles on the reforming and combustion channel axes are compared at different times from the reactants introduction. It appears that either in the reforming or in the combustion channel the temperatures in the center of the reactor are higher than those at both ends. Figure 5 also shows that the catalyst lights off locally around the central part of the catalytic slab. However, due to the limited number of measurement points, the individuation of a more accurate temperature profile was not possible and, therefore, a more marked variation of the temperatures along the reactor axis cannot be excluded. Such a long transient is not uncommon in the literature and already found by some authors when studying combustion of higher hydrocarbons in systems involving a microstructure-like configuration.[42,43]

In addition, data in Figure 5 point out that temperatures within the reforming channel are always higher than the corresponding temperatures within the combustion channels, indicating that a net heat flux out of the reactor is established. These findings are independent of the time, i.e., the relative values of the temperatures within a channel and, also, the relative values of the temperatures within a channel with respect to those in the

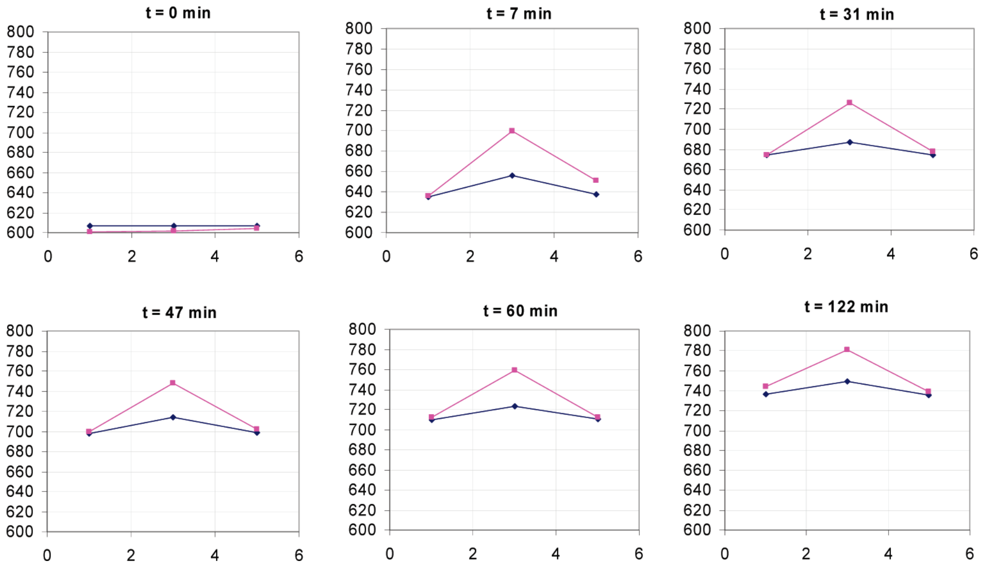

Figure 5. Longitudinal reactor temperature profiles at different times after fuel introduction ($t = 0$ min). Steam to methane molar ratio = 3, oxygen to methane molar ratio = 1.68. Each plot shows the temperature profile on the axis of the combustion (blue line) and of the reforming (red line) channel. Abscissa and ordinate refer to the position from the reactor inlet (cm) and to the temperature (°C), respectively.

adjacent channel remain practically the same, even though their absolute values change.

The results presented above deserve further discussion. Indeed, the fact that the measured temperatures in the reforming channel are always higher than the corresponding measured temperatures within the combustion channels is apparently incoherent. Being on the whole the reforming reactions endothermic, it is thermodynamically impossible that the temperature of the reacting zone is higher than the temperature of the corresponding reacting zone of the exothermic reaction (combustion). However, it must be recognized that the measured temperatures are not those of the reacting zones of the reactor, which coincide with the catalyst layers, but those of the gas on the channels' axes, as shown in Figure 2c. This appears evident from Figure 6 where the comparison between calculated transverse temperature profiles at three distances from the reactor inlet and the measured temperatures on the axis of each channel at the same distances is reported. From this figure it is evident that at each considered distance from the reactor inlet the reacting combustion zone is always at higher temperature than the corresponding reacting reforming zone. In contrast, gas temperature in the reforming channel may be higher or lower than that in the combustion channel at corresponding distances.

In addition to the discussion above it must be considered that the thermocouples measurement may be affected by error because of conductive and radiative heat transfer with the channel walls, which makes the temperature value dependent on that of the boundary of the channel and on the position of the sensing junction with respect to it. In particular, in the case of the combustion channels the thermocouples enter the channel from the reactor external cold wall and protrude for only 0.75 mm (Figure 2c). In this case the thermocouple measurement is markedly affected by conduction error, which lowers the temperature reading, and is fairly influenced by the radiation coming from the catalytic slab where the combustion reaction occurs. Instead, in the case of the thermocouples inserted in the reforming channel the influence of the conduction error is less pronounced because they protrude 5 mm inside the channel (Figure 2c) but are strongly affected by the radiation coming from the catalytic slabs. The temperature of the latter are, in the case of concurrent reactants feeding, for most of their length considerably higher than the gas temperature.[27,28] As a consequence, the temperature readings from the thermocouples in the combustion channels may slightly underestimate the actual gas temperature while readings from the thermocouples in the reforming channel should overestimate the real gas temperature.

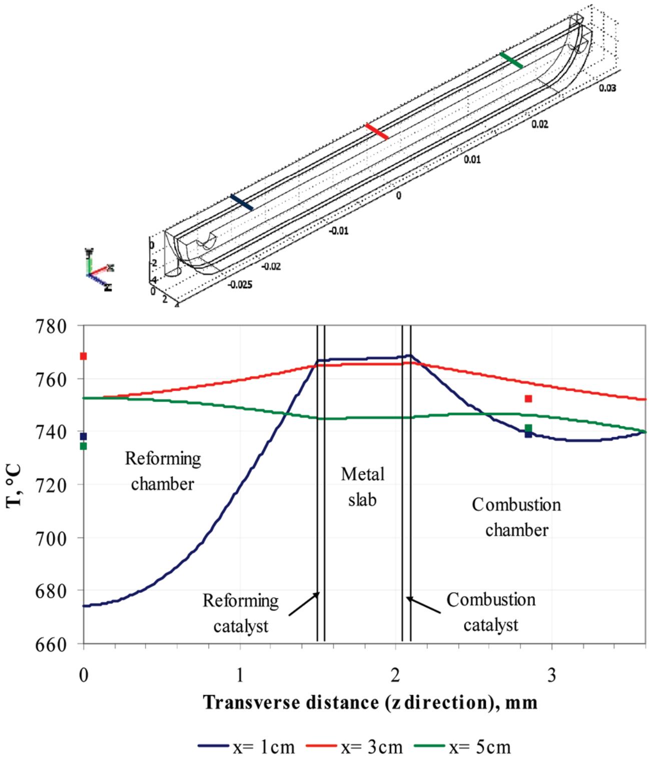

Figure 6. Comparison between calculated transverse temperature profiles (lines) at three distances from the reactor inlet (as indicated in the upper portion of the figure) and measured temperatures (points) on the axis of each channel at the same distances. Same colors refer to the same distances from the reactor inlet.

A numerical simulation was carried out to estimate the error of thermocouples readings through a model of thermocouples behavior in the same 3D configuration of this study, and where conductive, convective, and radiant heat transfer were considered. In particular, the radiative model "surface to surface" was

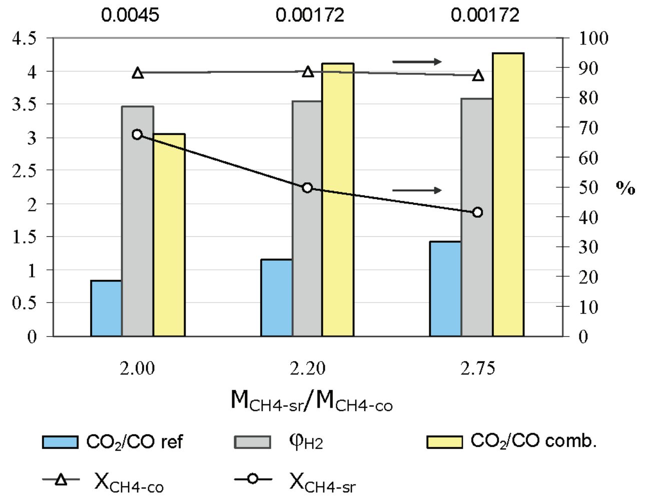

Figure 7. Reactor performance as a function of the feed ratio, $M_{\mathrm{CH4\text{-}sr}}/M_{\mathrm{CH4\text{-}co}}$, between the methane molar flow rates entering the steam reforming and the combustion channels, respectively. On the secondary x axis (head of the plot) for each test also the methane molar flow rate entering the combustion channel, $M_{\mathrm{CH4\text{-}co}}$, with the dimensions of mol/min, is reported. Molar feed ratio $O_2/CH_4 = 1.68$

applied neglecting the radiation absorbed or emitted by the gases. Results confirmed that combustion temperature sensors read values practically coincident with those of the external walls whereas reforming temperature sensors read values 10−15 K higher than the actual gas temperature when the catalytic walls temperature are 50−100 °C higher than the gas temperature.

In light of the considerations above it is worth observing the comparison, reported in Figure 6, between the calculated transverse temperature profiles and the measured temperatures on the axis of each channel. Indeed, it appears that, whatever the distance from the reactor inlet, on the axis of the combustion channel the measured temperatures are lower than those calculated and practically coincident with the calculated cold wall temperatures (dominance of the conduction error). Instead, on the axis of the reforming channel: at 1 cm from the reactor inlet the measured gas temperature is much higher than the calculated one but lower than the calculated reforming slab temperature; at 3 cm from the reactor inlet the measured gas temperature is higher than the calculated one and very close to the calculated reforming slab temperature; at 5 cm from the inlet the measured gas temperature is lower than the calculated one, likewise the calculated reforming slab temperature.

4.2. Steady State Behavior. The performance of the system under steady state for various inlet conditions is summarized in Figure 7 where results of tests carried out with different reactant flow rates are reported. In particular, defining $M_{\mathrm{CH4\text{-}sr}}$ and $M_{\mathrm{CH4\text{-}co}}$ as the methane molar flow rates entering the reforming and the combustion channels, respectively, data in Figure 7 refer to three tests performed with values of the ratio between $M_{\mathrm{CH4\text{-}sr}}$ and $M_{\mathrm{CH4\text{-}co}}$ equal to 2, 2.20, and 2.75. It is worth noting that such values were obtained varying both $M_{\mathrm{CH4\text{-}sr}}$ and $M_{\mathrm{CH4\text{-}co}}$ (when the ratio varies from 2 to 2.2) or just $M_{\mathrm{CH4\text{-}sr}}$ (when the ratio changes from 2.2 to 2.75). This can be evinced from the values of $M_{\mathrm{CH4\text{-}co}}$ reported on the head of Figure 7 as a secondary abscissa. The results show that, although the operating conditions are suitable for carrying out the coupled processes and that in any case φ_{H2} is > 3, the performance declines as the $M_{\mathrm{CH4\text{-}sr}}/M_{\mathrm{CH4\text{-}co}}$ ratio increases. This, in the case of the tests with $M_{\mathrm{CH4\text{-}sr}}/M_{\mathrm{CH4\text{-}co}}$ ratio increasing from 2 to 2.2, is a direct consequence of the relatively larger heat loss with respect to the heat generated by the methane combustion; whereas in the case of the tests with $M_{\mathrm{CH4\text{-}sr}}/M_{\mathrm{CH4\text{-}co}}$ ratio increasing from 2.2 to 2.75 depends on the higher heat amount absorbed by the reforming reactions due to the increase of $M_{\mathrm{CH4\text{-}sr}}$. Indeed, results in Figure 7 show that for all the tests $X_{\mathrm{CH4\text{-}co}}$ is very high and close to the theoretical maximum value, wih methane being in excess in the reacting mixture. Instead, as the relative amount of reforming reactants increases, $X_{\mathrm{CH4\text{-}sr}}$ decreases because the heat loss becomes proportionally more relevant (from 2 to 2.2) or the heat necessary to obtain a given conversion increases (from 2.2 to 2.7). This occurs although as the $M_{\mathrm{CH4\text{-}sr}}/M_{\mathrm{CH4\text{-}co}}$ ratio increases, the temperature of the system decreases as shown in Figure 8, which reports the reactor temperature profiles at steady state corresponding to the results shown in Figure 7.

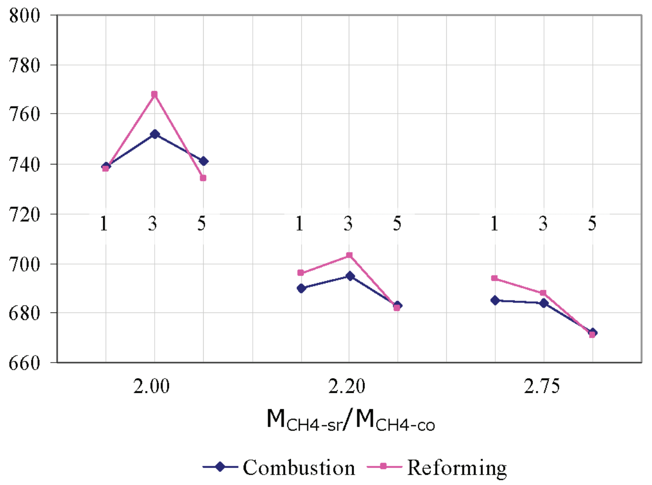

Figure 8. Temperature space profiles on the axes of the reforming and of the combustion channels at different $M_{\mathrm{CH4\text{-}sr}}/M_{\mathrm{CH4\text{-}co}}$ ratios. 1, 3, and 5 refer to thermocouples positions along the channel axis at 1, 3, and 5 cm, respectively, from the inlet.

Figure 8 also shows that at decreasing methane combustion flow rates or as the $M_{\mathrm{CH4\text{-}sr}}/M_{\mathrm{CH4\text{-}co}}$ ratio increases, the temperature profiles modify their shape. In particular, the maximum temperature moves from a location close to the reactor center (for $M_{\mathrm{CH4\text{-}sr}}/M_{\mathrm{CH4\text{-}co}} = 2$) toward the reactor inlet producing in the case of $M_{\mathrm{CH4\text{-}sr}}/M_{\mathrm{CH4\text{-}co}} = 2.75$ decreasing temperature profiles without a maximum.

A feature of the catalytic combustion, carried out in this work, is that the reaction products in spite of the presence of catalyst, which should favor the complete combustion, contain CO and H_2. Figure 7 clearly shows that the amount of CO at steady state vary from 0.25 to 0.3 of the CO_2 amount while the H_2 molar fraction on a dry basis is about 3.5%. This is not surprising considering that, as stated in Section 3.2, the combustion system operates under fuel-rich conditions. Indeed, the methane excess approximates the reacting system to a partial oxidation rather than a complete methane oxidation.

An open question in methane partial oxidation is the reaction mechanism and product development in the catalyst under fuel-rich conditions. Direct and indirect mechanisms were proposed.[44,45] The direct mechanism assumes that H_2 and CO are primary reaction products formed in the presence of gas-phase O_2 according to eq 4, which includes also the competitive formation of H_2O and CO_2.

$$CH_4 + \left(2 - \frac{x}{2} - \frac{y}{2}\right)O_2 \rightarrow xH_2 + yCO + (2 - x)H_2O + (1 - y)CO_2 \quad (0 \le x \le 2; 0 \le y \le 1) \qquad (4)$$

Table 2. Comparison between Experimentally Determined Performance of the Nonadiabatic Reactor and Those Predicted by the 2D and the 3D Models

	φ_{H2}	$X_{CH4\text{-}sr}$ (%)	$X_{CH4\text{-}co}$ (%)	y_{H2}	y_{CH4}	y_{CO}	y_{CO2}
experimental values	3.45	67.34	88.25	65.49	9.25	10.33	8.76
3D model ($\Delta H = -660$ kJ/mol)	3.32	68.6	89.72	68.6	10.1	14.5	6.75
3D model ($\Delta H = -803$ kJ/mol)	3.31	69.09	90.21	68.99	9.57	14.81	6.62
2D model ($\Delta H = -660$ kJ/mol)	3.23	84.77	83.53	72.7	4.1	17.68	5.53
2D model ($\Delta H = -803$ kJ/mol)	3.18	96.18	90.03	74.62	0.94	19.98	4.46

On the contrary, the indirect mechanism postulates a two-zone model with strongly exothermic CH_4 combustion to H_2O and CO_2, followed by strongly endothermic steam- and CO_2-reforming.[46−48]

$$CH_4 + 2O_2 \rightarrow CO_2 + 2H_2O, \quad \Delta H_r^\circ = -803 \text{ kJ/mol} \tag{5}$$

$$CH_4 + H_2O \rightarrow CO + 3H_2, \quad \Delta H_r^\circ = 206 \text{ kJ/mol} \tag{6}$$

$$CH_4 + CO_2 \rightarrow 2CO + 2H_2, \quad \Delta H_r^\circ = 247 \text{ kJ/mol} \tag{7}$$

This mechanism agrees with the work of Horn et al.,[49] where a comparison between Rh and Pt catalyzed partial oxidation of methane in an adiabatically operated metal coated foam was performed. For both catalysts a short oxidation zone formed at the catalyst entrance followed by a longer steam-reforming zone. Others authors postulated a mechanism in between.[32,49]

In any case, on the basis of the products experimental composition, the selectivities to H_2 and CO can be calculated and the values of x and y in eq 4 can be estimated. In our combustion tests, carried out under fuel-rich conditions, it was found that the products distribution was dependent on temperature and, then, different values for the x and y coefficients could be evaluated according to eqs 5 and 6, i.e.:

$$CH_4 + 1.82O_2 \rightarrow 0.17H_2 + 0.19CO + 1.83H_2O + 0.81CO_2 \quad (T = 700\ ^\circ C) \tag{8}$$

$$CH_4 + 1.729O_2 \rightarrow 0.30H_2 + 0.26CO + 1.70H_2O + 0.74CO_2 \quad (T = 752\ ^\circ C) \tag{9}$$

In addition, on the basis of the products distribution, it is possible to calculate for the reactions 8 and 9 the associated heat of reaction. In particular, for the reaction 8 $\Delta H^\circ_r = -708$ kJ/mol and for the reaction 9 = −657 kJ/mol.

As evident from these results, the incomplete combustion or the reforming of part of the combustion products, due to the fuel-rich fed mixture, led to a significant decrease of the heat generated per mole of converted methane (in the case of eq 9 of about 20%) with respect to the quantity generated with the complete combustion. This is important when considering thermal balances and system modeling, as discussed in Section 4.3.

4.3. Comparison between Experiments and Simulations. The comparison between the experimental results and the model predictions at steady state of a test carried out feeding the reactor with the molar rates reported in Table 1 and with an initial reactor temperature of 600 °C, are shown in Table 2 and in Figure 9. Specifically, the Table presents the product gas composition at the reforming channel outlet, the methane conversion both in the reforming and in the combustion channel, and the H_2 yield, as defined in Section 3.2. Figure 9, instead, shows the measured and the calculated temperature profiles along the channels axes. Actually, in Table 2 there are several model results and, in particular, two set of results for the 2D model and two set of results for the 3D model. For both models calculations were carried out assuming for the combustion the heat of reaction of the complete oxidation (eq 5) or the heat of reaction of the partial oxidation (eq 9). From data in Table 2 it is evident that the 3D model is capable of approximating experimental results with good accuracy, whereas the results of the 2D model deviate markedly from experimental findings, largely overestimating the methane conversion on the reforming side. In addition, the 3D model with the heat of reaction of the partial oxidation approaches the measured values better than that with the heat of reaction of the total oxidation.

Similar considerations can be drawn when comparing the experimental and the calculated reactor temperature space profiles in Figure 9. In particular, the 3D model describes with noticeable accuracy the measured temperatures in the combustion and in the reforming channels except the value in the reforming channel at 1 cm from the reactor inlet. On the contrary, the 2D model strongly overestimates the reforming channel temperature especially in the second half of the reactor.

In a previous work the authors compared the simulation results of both the 2D and the 3D models for given operating conditions.[28] In all the simulated cases the reactor was assumed to be adiabatic. In particular, they compared the temperature distribution over a slice of the 3D geometry lying on an $x-z$ plane intersecting the reactor in the middle of its height along y (see Figure 2) with that obtainable with a simulation performed through the 2D model. The comparison showed that the reactor temperature longitudinal profiles on the centerlines of the combustion and the reforming channels, and on the centerlines of the combustion and reforming catalysts, calculated with the 3D model and with the corresponding 2D model appeared closely similar, although some minor differences, which reflected a slightly better overall performance of the 3D reactor with respect to the 2D, could be noted.[28]

Quantitative comparisons between the 2D and 3D simulations were also made under various operating conditions. It appeared that, in general, the methane conversions at the reactor outlet,

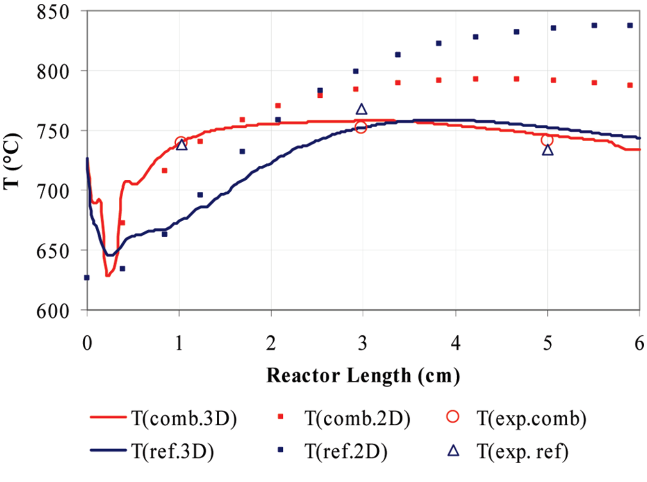

Figure 9. Comparison between the experimental temperature profiles on the axes of the reforming and combustion channels and the corresponding profiles simulated with the 2D and the 3D models.

calculated with the 2D model in both the combustion and reforming channels, were slightly lower than that computed with the corresponding 3D model. This finding reflected the differences in the thermal behavior cited above. In any case, the methane conversions calculated with the 2D and the 3D models differed by less than 5%.[28]

Results presented in this paper complement such conclusions demonstrating that in the case of a nonadiabatic reactor the difference between the results of the 2D and the 3D model may be significant. This is because necessarily the 2D model cannot take into account the heat loss through the external surfaces perpendicular to the *y* direction in Figure 2.

5. Conclusion

Methane steam reforming coupled with methane catalytic combustion by direct heat transfer in a plate catalytic micro reactor was carried out and the reactor performance was successfully predicted by a 3D model.

The analysis of temperature distributions within the reactor channels evidenced a very long (100 min) reactor thermal transient, determined by the heat up of the whole reactor.

In contrast, the analysis of the reaction products distribution after catalyst ignition indicated that in both combustion and reforming sections catalysts undergo to a much shorter transient (about 40 min) before reaching steady state conditions. Since the reactants conversion and the extent of the reaction are determined by the reaction zone temperature, this means that the reaction zone (catalytic layers) reaches the steady temperature much faster than the whole reactor.

Results obtained with the 2D and 3D models under the same operating conditions evidenced marked differences in the assessment of the reactor performance. In particular, when the reactor operates under real conditions (nonadiabatic) a 3D model is needed to accurately predict the reactor performance since a 2D model, although much less time-consuming, cannot allow for the whole heat loss thereby yielding unreliable results.

Literature Cited

(1) Thormann, J.; Pfeifer, P.; Kunz, U.,; Schubert, K. Reforming of Diesel Fuel in a Micro Reactor. *Int. J. Chem. Reactor Eng.* **2008**, *6*, Presentation P1.

(2) Barrai, F.; Castaldi, M. J. Experimental Investigation of a JP8 Fuel Processor: Autothermal Reformer and CO-Cleanup Train. *Ind. Eng. Chem. Res.* **2010**, *49*, 1577–1587.

(3) Ahmed, S.; Ahluwalia, R.; Lee, S. H. D.; Lottes, S. A gasoline fuel processor designed to study quick-start performance. *J. Power Sources* **2006**, *154*, 214–222.

(4) Gould, B. D.; Chen, X.; Schwank, J. W. Dodecane reforming over nickel-based monolith catalysts. *J. Catal.* **2007**, *250*, 209–221.

(5) Kang, I.; Bae, J. Autothermal reforming study of diesel for fuel cell application. *J. Power Sources* **2006**, *159*, 1283–1290.

(6) Liut, D.-J.; Kaun, T. D.; Liao, H. K. H.-K.; Ahmed, S. Characterization of kilowatt-scale autothermal reformer for production of hydrogen from heavy hydrocarbons. *Int. J. Hydrogen Energy* **2004**, *29*, 1035–1046.

(7) Nilsson, M.; Karatzas, X.; Lindstrom, B.; Pettersson, L. J. Assessing the adaptability to varying fuel supply of an autothermal reformer. *Chem. Eng. J.* **2008**, *142*, 309–317.

(8) Williams, K.; Schmidt, L. Catalytic autoignition of higher alkane partial oxidation on Rh-coated foams. *Appl. Catal., A* **2006**, *299*, 30–45.

(9) Lee, I. C. Rhodium supported on thermally enhanced zeolite as catalysts for fuel reformation of jet fuels. *Catal. Today* **2008**, *136*, 258–265.

(10) Dreyer, B.; Lee, I.; Krummenacher, J.; Schmidt, L. Autothermal steam reforming of higher hydrocarbons: *n*-decane, *n*-hexadecane, and JP-8. *Appl. Catal., A* **2006**, *307*, 184–194.

(11) Cheekatamarla, P. K.; Finnerty, C. M. Synthesis gas production via catalytic partial oxidation reforming of liquid fuels. *Int. J. Hydrogen Energy* **2008**, *33*, 5012–5019.

(12) Strohm, J.; Zheng, J.; Song, C. Low-temperature steam reforming of jet fuel in the absence and presence of sulfur over Rh and Rh-Ni catalysts for fuel cells. *J. Catal.* **2006**, *238*, 309–320.

(13) Hartmann, M.; Kaltschmitt, T.; Deutschmann, O. Catalytic partial oxidation of higher hydrocarbon fuel components on Rh/Al$_2$O$_3$ coated honeycomb monoliths. *Catal. Today* **2009**, *147S*, S204–S209.

(14) Farrauto, R. J.; Liu, Y.; Ruettinger, W.; Ilinich, O.; Shore, L.; Giroux, T. Precious metal catalysts supported on ceramic and metal monolithic structures for the hydrogen economy. *Catal. Rev. Sci. Eng.* **2007**, *49*, 141–196.

(15) Farrauto, R. J. The generation of hydrogen for the solid polymer membrane fuel cell. *C. R. Acad. Sci., Ser. IIC* **2000**, *3*, 573–575.

(16) Dorazio, L.; Castaldi, M. J. Autothermal reforming of tetradecane (C14H30): A mechanistic approach. *Catal. Today* **2008**, *136*, 273–280.

(17) Roychoudhury, S.; Castaldi, M.; Lyubovsky, M.; LaPierre, R.; Ahmed, S. Microlith catalytic reactors for reforming iso-octane-based fuels into hydrogen. *J. Power Sources* **2005**, *152*, 75–86.

(18) Ahmed, S.; Krumpelt, M. Hydrogen from hydrocarbon fuels for fuel cells. *Int. J. Hydrogen Energy* **2001**, *26*, 291–301.

(19) Zanfir, M.; Gavriilidis, A. Catalytic Combustion Assisted Methane Steam Reforming. *Chem. Eng. Sci.* **2003**, *58*, 3947–3960.

(20) Robbins, F. A.; Zhu, H.; Jackson, G. S. Transient modeling of combined catalytic combustion/CH$_4$ steam reformng. *Catal. Today* **2003**, *83*, 141–156.

(21) Kolios, G.; Gritsch, A.; Glo1ckler, B.; Sorescu, G. Novel Reactor Concepts for Thermally Efficient Methane Steam Reforming: Modeling and Simulation. *Ind. Eng. Chem. Res.* **2004**, *43*, 4796–4808.

(22) Cao, C.; Wang, Y.; Rozmiarek, R. T. Heterogeneous reactor model for steam reforming of methane in a microchannel reactor with microstructured catalysts. *Catal. Today* **2005**, *110*, 92–97.

(23) Avci, A. K.; Trimm, D. L.; İlsen Önsan, Z. Heterogeneous reactor modeling for simulation of catalytic oxidation and steam reforming of methane. *Chem. Eng. Sci.* **2001**, *56*, 641–649.

(24) Frauhammer, J.; Eigenberger, G.; Hippel, L. v.; Arntz, D. A new reactor concept for endothermic high-temperature reactions. *Chem. Eng. Sci.* **1999**, *54*, 3661–3670.

(25) Zanfir, M.; Gavriilidis, A. Modelling of a catalytic plate reactor for dehydrogenation-combustion coupling. *Chem. Eng. Sci.* **2001**, *56*, 2671–2683.

(26) Kolios, G.; Frauhammer, J.; Eigenberger, G. Effcient reactor concepts for coupling of endothermic and exothermic reactions. *Chem. Eng. Sci.* **2002**, *57*, 1505–1510.

(27) Vaccaro, S., Ciambelli, P. Modeling of Surface-bed Reactor for Endothermic and Exothermic Reactions Coupling. Ch. 30 in *Recent Advances in Modelling and Simulation*, Petrone, G., Cammarata, G., Eds.; I-Tech Education and Publishing: Wien, Austria, 2008; pp 580−605.

(28) Vaccaro, S.; Malangone, L.; Ciambelli, P. Modelling of a Catalytic Micro-Reactor Coupling Endothermic Methane Reforming and Combustion. *Int. J. React. Eng.* **2010**, *8*, A51.

(29) Ugues, D.; Specchia, S.; Saracco, G. Optimal Microstructural Design of a Catalytic Premixed FeCrAlloy Fibre Burner for Methane Combustion. *Ind. Eng. Chem. Res.* **2004**, *43* (9), 1990–1998.

(30) Xu, J.; Froment, G. F. Methane steam reforming, methanation and water-gas shift. I. Intrinsic kinetics. *AIChE J.* **1989**, *35*, 88–96.

(31) Hou, K.; Hughes, R. The kinetics of methane steam reforming over a Ni/α-Al$_2$O$_3$catalyst. *Chem. Eng. J.* **2001**, *82* (1−3), 311–328.

(32) Deutschmann, O. Computational Fluid Dynamics Simulation of Catalytic Reactors. I. In *Handbook of Heterogeneous Catalysis*, 2nd ed., Wiley-VCH: Weinheim, 2008; pp 1811−1828.

(33) Perry, J. H., Green, D. W., Maloney, J. O. *Perry's Chemical Engineer's Handbook*, 7th ed.; McGraw Hill: New York, 1997.

(34) Ciambelli, P.; Malangone, L.; Manna, M. A.; Vaccaro, S. Experimental Investigation of coupling of endo and exothermic reactions in a catalytic microstructured reactor. *Chem. Eng. Trans.* **2009**, *17*, 157–162,; doi: 10.3303/CET0917027.

(35) Cullis, C. F.; Willatt, B. M. Oxidation of methane over supported precious metal catalysts. *J. Catal.* **1983**, *83*, 267–285.

(36) Cullis, C. F.; Keene, D. E.; Trimm, D. L. Pulse flow reactor studies of the oxidation of methane over palladium catalysts. *Trans. Faraday Soc.* **1971**, *67*, 864–876.

(37) Yao, Y.-F. Y. Oxidation of alkanes over noble metal catalysts. *Ind. Eng. Chem. Prod. Res. Dev.* **1980**, *19*, 293–298.

(38) Garetto, T. F.; Apesteguia, C. R. Oxidative catalytic removal of hydrocarbons over Pt/Al$_2$O$_3$ catalyst. *Catal. Today* **2000**, *62*, 189–199.

(39) Otto, K. Methane oxidation over Pt on gamma-alumina: kinetics and structure sensitivity. *Langmuir* **1989**, *5*, 1369–1374.

(40) Niwa, M.; Awano, K.; Muratami, Y. Activity of supported platinum catalysts for methane oxidation. *Appl. Catal.* **1983**, *7* (3), 317–325.

(41) Kolaczkowski, S. Y.; Serbetcioglu, S. Development of combustion catalysts for monolith reactors: a consideration of transport limitations. *Appl. Catal., A* **1996**, *138*, 199–214.

(42) Barrai, F.; Castaldi, M. J. Experimental Investigation of a JP8 Fuel Processor: Autothermal Reformer and CO-Cleanup Train. *Ind. Eng. Chem. Res.* **2010**, *49*, 1577–1587.

(43) Shakir, O.; Yezerets, A.; Currier, N. W.; Epling, W. S. Spatially resolving concentration and temperature gradients during the oxidation of propylene on Pt/Al_2O_3. *Appl. Catal., A* **2009**, *365*, 301–308.

(44) York, A. P. E.; Xiao, T.; Green, M. L. H. Brief Overview of the Partial Oxidation of Methane to Synthesis Gas. *Top. Catal.* **2003**, *22*, 345–358.

(45) Weng, W. Z.; Chen, M. S.; Yan, Q. G.; Wu, T. H.; Chao, Z. S.; Liao, Y. Y.; Wan, H. L. Mechanistic study of partial oxidation of methane to synthesis gas over supported rhodium and ruthenium catalysts using in situ time-resolved FTIR spectroscopy. *Catal. Today* **2000**, *63*, 317–326.

(46) Souza, M. M. V. M.; Schmal, M. Autothermal reforming of methane over Pt/ZrO_2/Al_2O_3 catalysts. *Appl. Catal., A* **2005**, *281*, 19–24.

(47) Tavazzi, I.; Beretta, A.; Groppi, G.; Forzatti, P. Development of a molecular kinetic scheme for methane partial oxidation over a Rh/α-Al_2O_3 catalyst. *J. Catal.* **2006**, *241*, 1–13.

(48) Horn, R.; Williams, K. A.; Degenstein, N. J.; Bitsch-Larsen, A.; Dalle Nogare, D.; Tupy, S. A.; Schmidt, L. D. Methane catalytic partial oxidation on autothermal Rh and Pt foam catalysts: Oxidation and reforming zones, transport effects, and approach to thermodynamic equilibrium. *J. Catal.* **2007**, *249*, 380–393.

(49) Lyubovsky, M.; Roychoudhury, S.; LaPierre, R. Catalytic partial "oxidation of methane to syngas" at elevated pressures. *Catal. Lett.* **2005**, *99*, 113–117.

Received for review March 2, 2010
Revised manuscript received May 29, 2010
Accepted June 2, 2010

IE100464B